

Learned Focused Plenoptic Image Compression with Microimage Preprocessing and Global Attention

Kedeng Tong, Xin Jin*, *Senior Member, IEEE*, Yuqing Yang, Chen Wang, Jinshi Kang, Fan Jiang

Abstract—Focused plenoptic cameras can record spatial and angular information of the light field (LF) simultaneously with higher spatial resolution relative to traditional plenoptic cameras, which facilitate various applications in computer vision. However, the existing plenoptic image compression methods present ineffectiveness to the captured images due to the complex micro-textures generated by the microlens relay imaging and long-distance correlations among the microimages. In this paper, a lossy end-to-end learning architecture is proposed to compress the focused plenoptic images efficiently. First, a data preprocessing scheme is designed according to the imaging principle to remove the sub-aperture image ineffective pixels in the recorded light field and align the microimages to the rectangular grid. Then, the global attention module with large receptive field is proposed to capture the global correlation among the feature maps using pixel-wise vector attention computed in the resampling process. Also, a new image dataset consisting of 1910 focused plenoptic images with content and depth diversity is built to benefit training and testing. Extensive experimental evaluations demonstrate the effectiveness of the proposed approach. It outperforms intra coding of HEVC and VVC by an average of 62.57% and 51.67% bitrate reduction on the 20 preprocessed focused plenoptic images, respectively. Also, it achieves 18.73% bitrate saving and generates perceptually pleasant reconstructions compared to the state-of-the-art end-to-end image compression methods, which benefits the applications of focused plenoptic cameras greatly. The dataset and code are publicly available at <https://github.com/VincentChandelier/GACN>.

Index Terms—Focused plenoptic camera, plenoptic image coding, learned image compression, global attention.

I. INTRODUCTION

THE focused plenoptic camera [1] is the second generation of plenoptic cameras, which can record the four-dimensional (4D) light field (LF) with higher spatial resolution. Comparing to the traditional plenoptic cameras [2], so-called plenoptic 1.0 cameras, which place the

microlens array (MLA) at the image plane of the main lens, as shown in Fig. 1(a), to record the rays coming from each object point by the pixels beneath each microlens, as shown in Fig. 2(a), focused plenoptic cameras, as shown in Fig. 1(b), build a relay imaging architecture by putting the MLA at a distance of a behind the image plane of the main lens to re-image the main lens image at different angles. Each microlens in it works like a virtual camera to capture a portion of the main lens image from a perspective to form a microimage, e. g. the 69×69 circular regions shown in Fig. 2(b) that are captured by Tsinghua Single-focused Plenoptic Camera (TSPC) [3], and neighboring microimages record the object points from different perspectives to preserve the angular information. So, it achieves a/b times higher LF spatial resolution compared to the traditional plenoptic cameras [1], where b is the distance from MLA to the sensor in Fig. 1(b). Combining with its portability, the focused plenoptic camera becomes one of the promising acquisition devices in 3D reconstruction, industrial inspection, and 6-degree-of-freedom virtual reality [4], which draws great attention both from academy and industry to compress the images captured by them efficiently. ISO/IEC JTC 1/SC 29/WG 04 established an ad hoc group of lenslet video coding [5, 6] to study the compression techniques for it. JPEG PLENO [7] also starts to analyze the data for standardization. However, efficient compression is still challenging because of the distinct pixel distribution features in the focused plenoptic images.

Comparing the features in the focused plenoptic image and those in the traditional plenoptic image for the same scene in Fig. 2, significant distribution differences can be found. As shown in the magnifications of the wheel, each microimage in the focused plenoptic image (Fig. 2(b)) is much larger than that in the traditional plenoptic image (Fig. 2(a)) because of the relay imaging architecture and each of them images the wheel from a different perspective, which makes the textures inside the microimage more complex than those in traditional plenoptic microimage. Since the views of the wheel are recorded by the neighboring microimages, as shown in Fig. 2(b), and the size of the microimage is big, the neighboring microimages present long-distance spatial correlations. These differences make hybrid coding tools like local prediction [8-16] ineffective in exploiting the spatial correlations while preserving the details simultaneously. Although some image-principle-guided compression methods [17-20] were proposed to generate the spatial predictor by block-wise zooming and interpolation, blocking artifacts may be introduced to the regions with detailed textures, which limits the compression performance. The sub-aperture/pseudo-video-based coding techniques [21-33] are not universal to focused plenoptic images because of the irreversibility of converting sub-aperture images back to the focused plenoptic images [1, 17]. And, learning-based image compression techniques [34-37] present ineffectiveness because

The work was supported in part by National Natural Science Foundation of China under Grant No. 62131011, and Shenzhen Project under Grant No. JCYJ20200109142810146.

The authors are with the Shenzhen International Graduate School, Tsinghua University, Shenzhen 518055, China (e-mail:tkd20@mails.tsinghua.edu.cn; jin.xin@sz.tsinghua.edu.cn; yangyq22@mails.tsinghua.edu.cn; wang-che20@mails.tsinghua.edu.cn; kjs20@mails.tsinghua.edu.cn; jf19@mails.tsinghua.edu.cn).

of the limited receptive field and the incompatibility between the network trained on the continuous textures in the square patches of the natural images and the textural discontinuities in hexagonally arranged microimages.

So, in this paper, a lossy end-to-end learning architecture is proposed to compress the focused plenoptic images efficiently. First, based on the observations that inter-microimage pixels, boundary incomplete microimages, and vignetting pixels in the microimages are ineffective in light field applications, like refocusing, rendering, etc., a sub-aperture image lossless preprocessing scheme is proposed to reshape the sub-aperture image effective pixels in each microimage and align the cropped microimages to the rectangular grid to be compatible with patch-based training and to reduce the pixel redundancy. Then, a global attention module with large receptive field is proposed to capture the long-distance correlations among the feature maps in the resampling process to improve compression efficiency. The query derived from the down-sampling/up-sampling feature map computes pixel-wise vector attention with the key-value pairs derived from the unsampled feature map, which makes the output of attention computing with a skip connection can draw global dependencies from the inputs. A dataset with 1910 focused plenoptic images captured by TSPC is proposed to benefit focused plenoptic image related learning applications. Extensive experimental results demonstrate that the proposed work can achieve an average of 62.57% and 51.67% bitrate reduction compared to HEVC and VVC intra coding, respectively, on 20 preprocessed plenoptic images. It also saves 18.73% bitrate relative to the state-of-the-art (SOTA) learned image compression models. It achieves SOTA performance on both peak signal-to-noise ratio (PSNR) and multi-scale-structural similarity index (MS-SSIM) in comparison with compressing the rendered sub-aperture images using HEVC inter coding. To the best of our knowledge, it is the first work that compresses focused plenoptic images directly while achieving competitive performance to sub-aperture image compression.

The remainder of this paper is organized as follows. Section II presents the related works on plenoptic image compression and learned image compression. Section III introduces the analysis of focused plenoptic images and the proposed data preprocessing scheme. Section IV introduces the proposed focused plenoptic image dataset. The learned image compression framework and the details are described in Section V. Experimental results and analysis are provided in Section VI followed by a conclusion drawn in Section VII.

II. RELATED WORKS

In this section, plenoptic image compression methods and learned image compression approaches are introduced.

A. Plenoptic Image Compression

The existing plenoptic image compression approaches can be mainly categorized into two groups: compressing the sub-aperture images rendered from the plenoptic image and compressing plenoptic images directly. Methods of the first category consider reordering or sparse sampling the sub-aperture images to be the pseudo-videos and utilize the inter-coding tools to exploit the correlations among the views for higher compression efficiency [21-33]. Reordering all

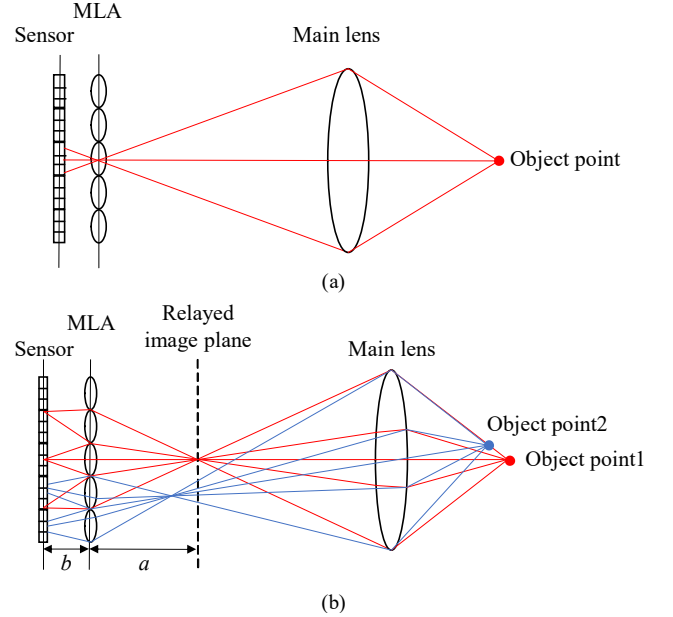


Fig. 1. Imaging principle of: (a) traditional plenoptic cameras; (b) focused plenoptic cameras. Red lines and blue lines represent the light rays coming from a focused object point and an unfocused object point, respectively.

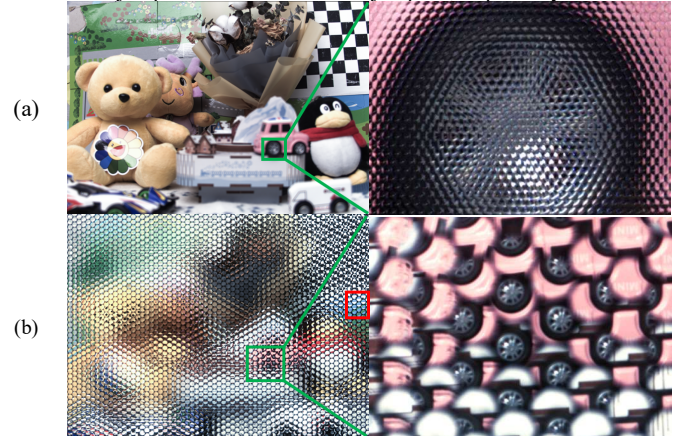


Fig. 2. Plenoptic images of a same scene captured by: (a) the traditional plenoptic camera; and (b) the focused plenoptic camera.

sub-aperture images into a pseudo-video sequence with zigzag [26], raster [28], spiral [27], and hierarchical [25, 31] scan orders have been exploited by the off-the-shelf codec to reduce the spatial and angular redundancy. Alves *et al.* [38] employed the 4D block partition, 4D transform, and 4D coefficient to encode the 4D sub-aperture images and proposed 4D-native hexadeca-tree-oriented bit-plane clustering to improve rate-distortion performance. Bakir *et al.* [21] proposed to encode the sparsely selected views and reconstruct the unselected views by the linear approximation at the decoder side. Huang *et al.* [22] transmitted the disparity maps additionally to geometrically predict the unselected views from the decoded views. Liu *et al.* [33] proposed three elaborate subnetworks to reconstruct and refine dense sub-aperture images at the decoder side. Although sub-aperture images can be extracted both from traditional and focused plenoptic images, it is irreversible to convert sub-aperture images back to the focused plenoptic image due to the relay imaging principle where patches of each microimages are interpolated and tiled to obtain the rendered

views [39, 40]. Thus, the sub-aperture image compression approaches that exploit the spatial-angular redundancy among the views limit the applications of the decoded focused plenoptic data [41].

The second group of plenoptic image compression methods directly encodes the images to reduce the spatial redundancy of the repetitive patterns among the adjacent macropixels/microimages [8-16, 42-44]. Locally linear embedding (LLE) [8] regards the current coding macropixels as the linear combination of the neighboring macropixels. The bi-directional self-similarity methods [9, 10] introduce two predictors derived from the adjacent macropixels for the current block and achieve impressive bitrate saving relative to HEVC. A two-stage high-order intra-prediction method [11] predicts each coding unit through the geometric transformation within the decoded region. The regression-based prediction method [12] proposes to classify the coding units into three categories based on the content property and design content-based weighted reference blocks to improve coding efficiency. Disparity correlation [13] and content depth [42] reveal that the depth of scenes is beneficial to find the imaging response blocks. Based on reshaping and aligning the macropixels with the rectangular grid to generate the plenoptic image with higher spatial correlation, the regularized macropixels compression approaches [14-16] improve the prediction efficiency by designing a single block or weighted multiblock prediction. The decorrelation network [44] utilizes the stride convolution and dilation convolution as specific feature extractors to decouple the spatial-angular information and the decoupled feature maps are compressed jointly to improve the compression efficiency of preprocessed traditional plenoptic images. However, these compression methods based on the short-distance spatial-angular correlation of macropixels are inevitably inapplicable and show ineffective compression performance for focused plenoptic images due to the long-distance spatial correlation and low internal redundancy in microimages.

Due to the different intensity distribution between traditional and focused plenoptic images, Li *et al.* [45] proposed a displacement intra-prediction scheme, which utilizes two reference blocks from the top and left microimages to predict the current coding unit. Image-correlated intra prediction (IIP) uses the matching blocks from the neighboring microimages, guided by the imaging principle of focused objects, as the weighted prediction for the current prediction unit (PU) to improve the compression efficiency [18]. Zoomed imaging-principle-guided prediction [17] determines the positions and scales of the prediction candidates according to the focusing status and the focal length of the microlens to improve the coding efficiency on multi-focused plenoptic images. Besides, the intra-block-copy mode of screen content coding extension (SCC) [46] shows efficiency in plenoptic image coding [18] due to the similar patterns among the adjacent microimages. However, artifacts may be introduced to the complex texture regions, which limits the compression efficiency subjectively and objectively.

B. Learned Image Compression

In recent years, a great surge of learned image compression approaches [34-37, 47-49] have been proposed and achieved an impressive trade-off between the bitrate and distortion

compared to compression standards including JPEG [50], JPEG2000 [51], HEVC [52] and VVC [53]. Ballé *et al.* [34] proposed a simple end-to-end network to compress the factorized latent representation using differentiable quantization. Ballé *et al.* [35] proposed a hyperprior network to model the distribution of latent representation. Minnen *et al.* [37] explored the context regression model as an auxiliary model to capture the spatial redundancy in the latent space. Mixture Gaussian distribution is explored in [36, 49, 54] to estimate the accurate distribution of latent representation to improve the compression efficiency. Cheng *et al.* [36] proposed a local attention module to generate the compact latent representation to enhance the performance. Zou *et al.* [47] designed the deep window-based attention to capture the local and global redundancy to reduce the bit consumption but reconstruct high-quality images. However, limited by receptive field and distinctive data redundancy, they are still inefficient in exploring the long-distance spatial correlations among the microimages and preserving the textures in the focused plenoptic images simultaneously.

III. FOCUSED PLENOPTIC IMAGE ANALYSIS AND PROPOSED DATA PREPROCESSING SCHEME

In this section, we propose the data preprocessing method based on pixel effectiveness analysis using geometric ray tracing.

A. Pixel Effectiveness Analysis

Because of the relay imaging process, the pixels under each microlens of the focused plenoptic camera record a portion of the scene from a perspective, which results in the pixel effectiveness in rendering the sub-aperture images at different viewpoints differing from those in traditional plenoptic image. To analyze the pixel effectiveness in sub-aperture image rendering, TSPC designed by us, which has been adopted by ISO/IEC [55] as one of the representative focused plenoptic image acquisition devices, is selected to facilitate the analysis. As illustrated in Fig. 1(b), TSPC inserts the MLA into the light path at a distance a behind the image plane of the main lens and distance b in front of the sensor, respectively, where a and b satisfy the Gaussian equation with the focal length f of the MLA. Using the magnified portion in the captured raw image as an instance in Fig. 3(a), we propose to classify the pixels into four categories according to their effectiveness in optical responses: **Inter-microimage Pixels**: To obtain the highest fill factor, circular microlenses are arranged hexagonally. The f -number of the main lens and the microlens is matched and the pixels under each microlens record the light rays refracting from the single microlens without cross-talk from other microlenses. Thus, the pixels located among the non-overlapping microimages, so-called inter-microimage pixels, are dark and are useless in reconstructing the recorded light field [56, 57], as shown in Fig. 3(a). These pixels are marked in black in Fig. 3(c), which takes up 9.3% of the total pixels and can be ignored in compression and transmission without loss of the spatial and angular information of the light field.

Boundary Incomplete Microimages: Since the size of the image sensor is generally not the integer multiples of the microlens, several incomplete microlens may exist at the boundary of the plenoptic image, under which boundary

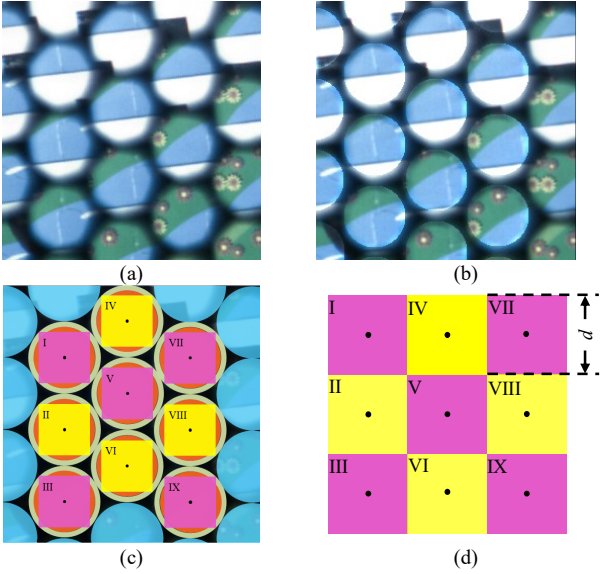


Fig. 3. Preprocessing for the 256×256 patch of the raw plenoptic image marked in the red rectangle in Fig. 2(b) as a toy example: (a) raw plenoptic image patch; (b) devignetted patch (a); (c) pixel classification of (b), in which inter-microimage pixels, boundary incomplete microimages, and vignetting pixels are marked in black, blue, and light green, respectively. The circular region denoted in orange contains light field effective pixels. The magenta and yellow areas covering sub-aperture image effective pixels are the pixels picked by our data preprocessing scheme; and (d) the plenoptic image patch after preprocessing, in which the magenta and yellow blocks correspond to those in (c) to show the relative position.

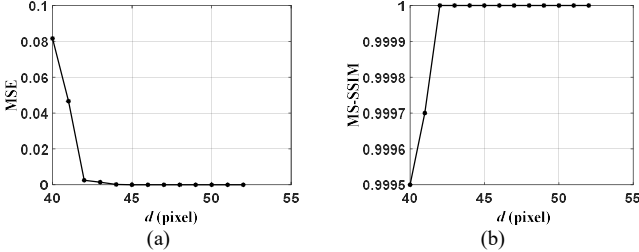


Fig. 4. Average distortion among 5×5 sub-aperture images with cutting size d . (a) Distortion measured with MSE. (b) Distortion measured with MS-SSIM.

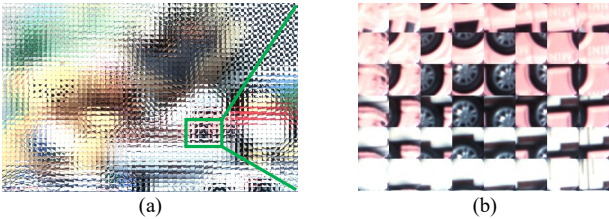


Fig. 5. Preprocessed plenoptic image and magnification. (a) Preprocessed plenoptic image. (b) Magnification of (a) in the green rectangle.

incomplete microimages are generated. Also, these regions generally record the light from the boundary of the main lens, which present low imaging quality. Like the regions marked in blue in Fig. 3(c), low imaging quality and insufficient spatial-angular information can be observed in Fig. 3(b) correspondingly, which cannot be used in subaperture image rendering. Taking the plenoptic images captured by TSPC as an example, the pixels of boundary incomplete microimages take about 8.3% of total pixels, which can be discarded in sub-aperture image rendering [39].

Vignetting Pixels: Since each microlens acts as a thin lens, as it

images a point away from the optical axis, the beam that can reach its image plane gradually becomes narrow due to the existence of a limited aperture, resulting in a gradual darkening effect around the periphery of the microimage, which generate so-called vignetting pixels as shown in Fig. 3(a). Although the white-image-based compensation methods [1, 40, 56] were proposed to mitigate this problem, the vignetting pixels marked in light green in Fig. 3(c) still suffer from non-negligible lens shading in the devignetted plenoptic image, as shown in Fig. 3(b), and are ineffective in sub-aperture image applications [58].

Sub-aperture Image Effective Pixels: Since the optical design and matching of f -number result in the circular exit pupil of the main lens and the microlens, the effective pixels area (EPA) underneath each complete microimages, where the light rays can reach the sensor with high energy and uniform light intensity distribution, record the reconstructive light field and are utilized for extracting the sub-aperture images from a single plenoptic image, denoted in orange in Fig 3 (c). Generally, the existing sub-aperture image conversion methods [1, 39, 40] select an inside square patch of the EPA of each microimage and tile the selected interpolated patches together to render a specific perspective. The size of selected patches depends on the depths of objects but does not exceed the size of the inscribed maximum square of EPA. In other words, sub-aperture image effective pixels located as in the inscribed maximum square of EPA are genuinely beneficial for sub-aperture image rendering.

According to the pixel effectiveness analysis, removing *Inter-microimage Pixels*, *Boundary Incomplete Microimages* and *Vignetting Pixels* will not influence the performance of sub-aperture image rendering that is mainly used in LF applications. But removing them can reduce the data amount greatly, which is beneficial to compression.

Additionally, it is found that microimages are arranged hexagonally in the plenoptic image according to the MLA layout. If we partition the plenoptic image into rectangular patches, like that generally used in the training/encoding process of end-to-end image compression [36, 37, 43, 49], massive incomplete microimages in the patches will introduce irregular intensity discontinuities, which directly harms the effectiveness of training and the feature extraction and results in low compression efficiency of transferring the existing the networks to the plenoptic images.

So, we propose a sub-aperture image lossless data preprocessing scheme by discarding the sub-aperture image ineffective pixels and reshaping the plenoptic image, which reduces data amount highly, benefits patch-based training, and does not sacrifice the LF application capabilities.

B. Proposed Data Preprocessing Scheme

The proposed data preprocessing scheme consists of two steps: *Microimage Cropping* and *Microimage Aligning*.

Microimage Cropping is to pick out sub-aperture image effective pixels in each microimages as the basic unit of preprocessed plenoptic images. Considering the imaging principle of focused plenoptic cameras and existing rendering methods, microimage cutting should guarantee the central pixel of each microimages is still the center of cropped microimage. Thus, taking the central pixels as the fixed reference points of each microimage, the square area is cropped with the cutting

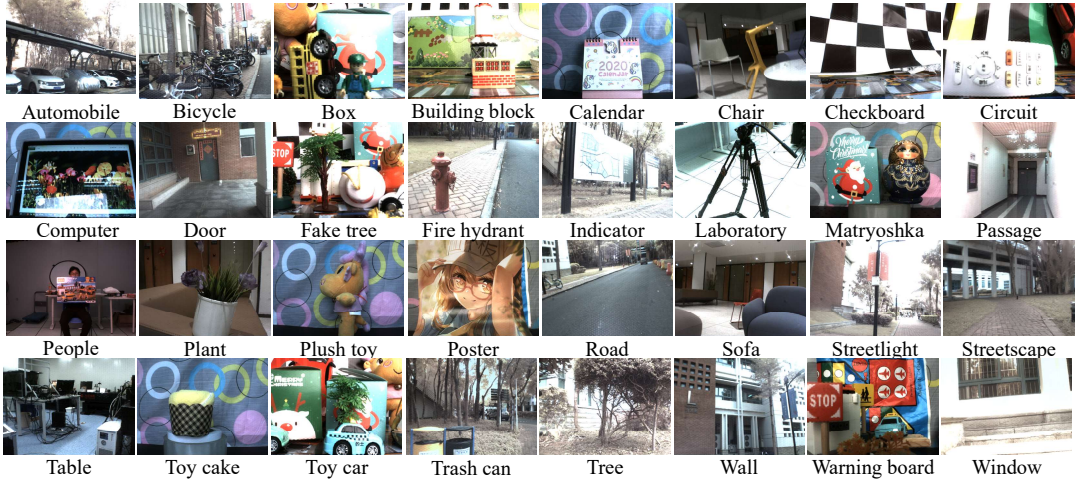


Fig. 6. Snapshot of the categories in the dataset. Each category is presented by the central view of a plenoptic image.

size d , as the yellow and magenta areas shown in Fig. 3(c). From the analysis of the above sub-aperture image effective pixels, d is given by:

$$d \geq d_{min} = \sqrt{2}mR, \quad (1)$$

where d_{min} , m and R are the length of minimum inscribed square, EPA radius coefficient, and the radius of microlens, respectively. Therefore, each complete microimage are processed into the $d \times d$ cropped microimages.

Microimage Aligning is to move the cropped microimages of the even column vertically to align them to the rectangular grid. The translation distance d_{td} is given by:

$$d_{td} = d / 2. \quad (2)$$

After *Microimage Cropping* and *Aligning*, the preprocessed plenoptic image in Fig. 3(c) becomes Fig. 3(d).

To demonstrate that the preprocessed data will not influence the sub-aperture image rendering performance, an analysis of the first frame in MPEG standard testing sequence ‘‘Cars’’ [59] is conducted by calculating the average distortion among the 5×5 sub-aperture images rendered from the original and those rendered from the preprocessed plenoptic image using the microimage stitching rendering tool [40]. m equals 0.8, white image compensation [60] is applied and R is set to 35 pixels according to the specification of microlens in TSPC. Mean square error (MSE) and MS-SSIM are used to measure the average distortion of sub-aperture images. The distortion statistics are retrieved and demonstrated in Fig. 4. The results reveal that when $d = 44 > d_{min} = 39.59$, the preprocessed plenoptic image is completely sub-aperture image lossless compared to the original plenoptic images.

The processed plenoptic images can be partitioned into rectangular patches to meet the needs of the deep compression network training and inference. Considering that the downsampling ratio used in the existing learned image compression is generally an integer multiple of 16 [36], the cutting size d is set as 48 pixels for TSPC plenoptic images in the preprocessing scheme. Therefore, the preprocessed image

Sensor	beA4000-62km (Basler)
SDK	Basler Pylon
Main lens	20 mm, f/2.8 aperture
Microlens focal length and f-number	4/3 mm, f/3.49
Number of microlens	69×51 , hexagonally packed
Number of complete microlens	66×42
Microlens diameter	381.6 μ m
Number of pixels beneath each microlens	69×69 pixels
Image sensor size	1/1.75 inch
Resolution of lenslet image after calibration as the original image	4080 (H) \times 3068 (V) 1.2 million pixels
Bit depth	8 bit
Color space	RGB

of Fig. 2(b) is shown in Fig. 5.

IV. PROPOSED FOCUSED PLENOPTIC IMAGE DATASET

To train a robust model, we propose a focused plenoptic image dataset ‘‘FPI2k’’¹ captured by TSPC. The specification of TSPC is listed in Table I.

To provide the data with content diversity, we capture real scenes indoor and outdoor with object depth variations. From a single plenoptic image, 5×5 sub-aperture images can be generated with much larger disparities one from the other. 1910 focused plenoptic images are captured and manually annotated to 32 categories based on their contents, as shown in Fig. 6. Each category selects the central view of a plenoptic image as an example to exhibit the properties of the dataset. The images taken indoors provide a large disparity among the views while objects in various depths are provided outdoors. A variety of contents and textures that do not exist in the existing datasets are included in our dataset, which greatly benefit robust algorithm training.

To the best of our knowledge, it is the first focused plenoptic image dataset with nearly 2000 images in the real circumstances.

¹ https://pan.baidu.com/s/1mVFoklr2Pf_wSyn4GAPEg?pwd=u15n

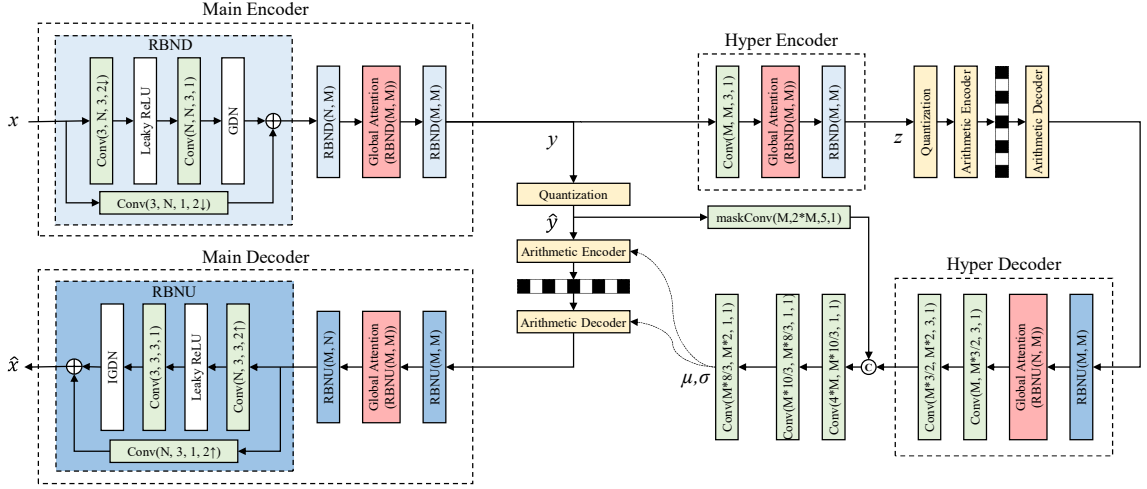


Fig. 7. The architecture of our proposed network with global attention module. *Conv*(*inch*, *outch*, *kernelsize*, *stride*) is a convolutional layer with the kernel size of $kernelsize \times kernelsize$ and a stride of *stride*. *Global Attention* (*conventionalnetwork*) represents the global attention module using *conventionalnetwork* as resampling network structure.

V. PROPOSED END-TO-END COMPRESSION NETWORK

Based on the proposed data preprocessing scheme and focused plenoptic image dataset, our end-to-end network accompanied by the global attention module is proposed.

A. Network Architecture

As depicted in Fig. 7, our network adopts a hierarchical hyperprior-context network [36] as the backbone, where the main encoder adopts 4 down-sampling operations mapping the given input x to the latent representation y . An auxiliary hyperprior autoencoder is used to capture the spatial corrections among y into side information z . Up-sampled quantized \hat{z} combined with a context model Cm is utilized to estimate the parameters of Gaussian distribution of each element of quantized latent representation \hat{y} for lossless entropy compression. Then the main decoder reconstructs the image \hat{x} by up-sampling \hat{y} . Following [36], residual bottleneck (RBN) structure with efficient receptive field is modified as RBN down-sampling (RBND) with stride convolution and RBN up-sampling (RBNU) with sub-pixel convolution in the encoder and decoder, respectively, to improve rate-distortion (RD) performance. Generalized divisive normalization (GDN) [34] and its inverse format IGDN, are used as the local normalization to remove statistical dependencies in RBN.

Considering the long-distance and pixel-wise redundancy among the microimages in plenoptic images, the third and first down-sampling/up-sampling networks in the main and hyperprior autoencoder are modified respectively with the proposed global attention module to extract the compact representations for better compression efficiency, as shown in Fig. 7.

Learned image compression aims to minimize the bitrate consumption and expected distortion \hat{x} respect to x . Therefore, the loss function is given by:

$$\mathcal{L} = \mathcal{R}(y) + \mathcal{R}(z) + \lambda \cdot \mathcal{D}(x, \hat{x}), \quad (3)$$

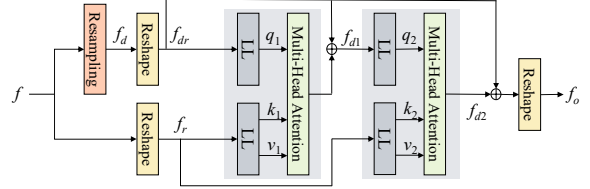


Fig. 8. Global attention module. The feature map f and resampled feature map f_d are reshaped into pixels-wise vector f_r and f_{dr} . The relevant latent vectors of f_{d1} are fetched with the multi-head global attention with the query q_1 derived from f_{dr} and the key k_1 , the value v_1 derived from f_r by linear layer. With 2 times global attention computing, resampling result f_o is obtained by reshaping output of attention f_{d2} back to multi-dimension. The global attention module is beneficial to capture the global information in down-sampling/up-sampling operations.

where λ is the Lagrange multiplier to control the trade-off between bitrate and distortion; $\mathcal{R}(\cdot)$ represents the bitrate; and $\mathcal{D}(x, \hat{x})$ is the distortion between input image x and reconstructed image \hat{x} .

B. Global Attention Module

Due to the noticeable long-distance and pixel-wise redundancy among the microimages from the imaging principle, the key point of improving focused plenoptic compression efficiency is to extract the compact feature map with a large receptive field. And for learned compression, the down-sampling operations generally cause information loss affecting the reconstruction quality.

To address this problem, we propose the global attention module with pixel-wise vector correlation to explore the global dependencies among input feature maps $f \in \mathbb{R}^{C \times H \times W}$ in the down-sampling/up-sampling process, where C , H , and W are the number of channels, the height, and the width, respectively. Since down-sampling process in the encoder and up-sampling extraction in the decoder are symmetric in the end-to-end network, we illustrate the global attention module in the

down-sampling manner without loss of generality.

The proposed global attention module is depicted in Fig. 8. First, down-sampled feature map $f_d \in \mathbb{R}^{C \times \frac{H}{2} \times \frac{W}{2}}$ is generated from f by a convolution layer with stride of 2 or other down-sampling network structures. Then, feature map f and f_d apply a regular reshaping strategy which merges the dimensions of height and width and permutes the channels dimension with merged height-width dimension to transform into pixel-wise vectors. And the global attention computing is utilized for explore the correlation between the reshaped feature maps $f_r \in \mathbb{R}^{HW \times C}$ and $f_{dr} \in \mathbb{R}^{\frac{HW}{4} \times C}$, The global attention computing can be expressed as:

$$\begin{aligned} q_1 &= LL(f_{dr}) \\ k_1, v_1 &= LL(f_r) \\ f_{d1} &= Softmax\left(\frac{q_1 k_1^T}{\sqrt{C}}\right) v_1 + f_{dr}, \end{aligned} \quad (4)$$

where the query $q_1 \in \mathbb{R}^{\frac{HW}{4} \times C}$ is derived from f_{dr} through the linear layer (LL); the key $k_1 \in \mathbb{R}^{HW \times C}$ and the value $v_1 \in \mathbb{R}^{HW \times C}$ are acquired from f_r . The global attention computing maps the query and the set of key-value pairs to the output in pixel-wise vector format. Thus, the global attention computing enables to generate the compact output f_{d1} by drawing the global dependencies of input f_r with a skip connection of f_{dr} . The capacity of attention is enhanced by the multi-head attention computing [61]. With 2 times global attention computing, the final output of global attention $f_{d2} \in \mathbb{R}^{\frac{HW}{4} \times C}$ adding with f_{dr} is reshaped back to the high dimensional feature map $f_o \in \mathbb{R}^{C \times \frac{H}{2} \times \frac{W}{2}}$. Thus, the long-distance content information among the feature map f is represented compactly in feature map f_o by the large receptive attention module to affect RD performance.

The global attention module uses RBND and RBNU as the resampling component in the encoder and decoder. Considering the data size of the proposed image dataset and the complexity of attention module, we only insert the global attention module in the third down-sampling/up-sampling stage of the main autoencoder and first down-sampling/up-sampling stage of the hyper autoencoder, as shown in Fig. 7.

VI. EXPERIMENTS AND ANALYSIS

In this section, the effectiveness of the proposed method is demonstrated by comparing with SOTA hybrid codecs and learned models. First, the implementation details and test conditions are described. Then, the rate-distortion results and qualitative results are provided and analyzed. Thirdly, ablation study is conducted in terms of the effectiveness of the global attention module.

A. Implementation Details

Training: For training, we use 1877 preprocessed plenoptic images in ‘‘FPI2k’’ from all categories, and sequentially crop

them into 75080 patches with the size of $384 \times 384 \times 3$. Each patch includes 8×8 complete cropped microimages. The number of channels N and M are set to 128 and 192 in Fig. 7, respectively. Our models are optimized using MSE as the distortion metric in Eq. (3). We trained 6 models in total with $\lambda = (0.1, 0.05, 0.025, 0.01, 0.005, 0.001)$. All the models are trained for 50 epochs using the Adam with a batch size of 4. The initial learning rate is set to 1×10^{-4} and dynamically reduced by ReduceLRonPlateau with the patience of 5.

Evaluation: For comparison, 2 plenoptic images, the first frames of *Cars* [59] and *Matryoshka* [62] in MPEG-I Visual test video sequences, and 18 images in ‘‘FPI2k’’ are selected as the test images. The test set does not overlap with the training set. In inference, the preprocessed plenoptic images are padded to the multiple of 384 with zero and cropped into 384×384 patches in learned compression for computational efficiency. 5×5 sub-aperture images are rendered from each reconstructed plenoptic image via the TSPC rendering tool [39]. All the central sub-aperture images of test images are shown in Fig. 9.

B. Test Conditions

To evaluate the effectiveness of the proposed method and data preprocessing scheme, we compare our method with hybrid intra-coding tools, learned image compression models, and sub-aperture image compression methods. Reference software HM-16.22 [63], HM-16.9_SCM8.0 [64], and VTM-10.0 [65] are selected as the intra coding tools on original and preprocessed plenoptic image compression for general hybrid standards: H.265/HEVC [52], HEVC Screen Content Coding Extension (SCC) [46], and H.266/VVC [53], respectively. The macropixel-based method co-located single-block prediction (CSP) mode [16] on HEVC SCC for traditional plenoptic image are chosen for original and preprocessed plenoptic image compression. The imaging-principle-based method [18] based on HEVC and zoomed imaging-principle-guided prediction using SCC profile [17] for focused plenoptic images are utilized for plenoptic image compression. Four learned compression methods, including the basic factorized network Ballé *et al.* [34], the hyperprior network Ballé *et al.* [35], joint context-hyperprior work Minnen *et al.* [37], and Cheng *et al.* [36] which is the first learned work surpassing VVC intra-coding, are selected for preprocessed plenoptic image compression comparison. All the learned image compression models adopt the same training and evaluation strategy as our method. The sub-aperture image reordering image compression of spiral scan order [27] and raster scan order [26] are compared on HM-16.22. In total, 17 testing cases are defined and tested, as listed in Table II. The resolution of plenoptic images, preprocessed plenoptic images and sub-aperture images are 4080×3068 , 3168×2016 , and $1149 \times 830 \times 5 \times 5$, respectively.

For a fair comparison, the common test conditions [5] in MPEG-I lenslet video coding is used to evaluate the effectiveness of testing cases for intra coding, learned image compression, and sub-aperture image compression. As depicted in Fig. 10, the distortions are measured with sub-aperture images rendered from original plenoptic images in RGB color space. The distortion between the reference sub-aperture images and the reconstructed sub-aperture images is measured by the average of PSNR or MS-SSIM of each sub-aperture image. The distortion calculation is given by:

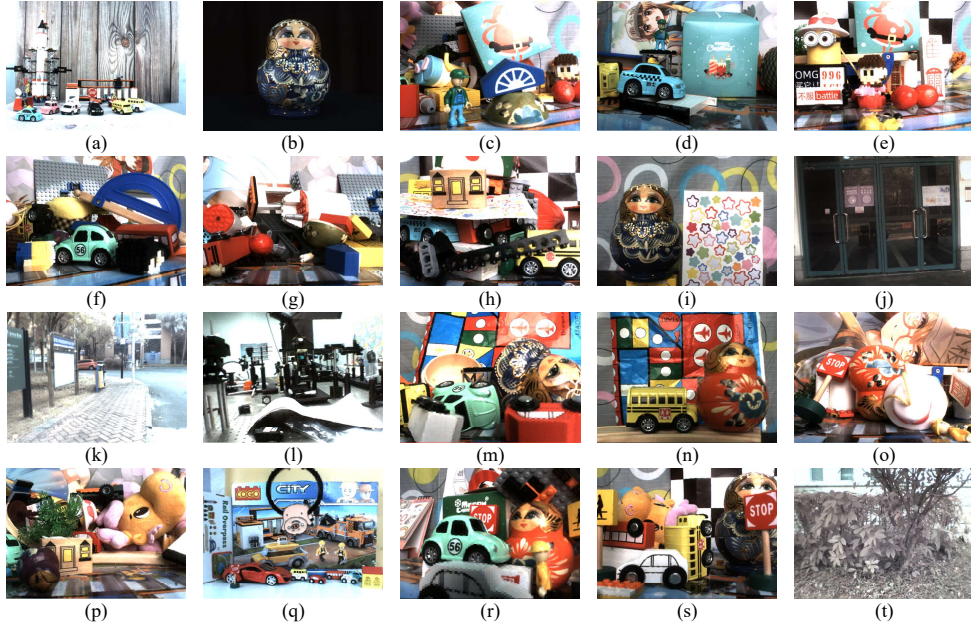


Fig. 9. Central views of 20 test images. (a) I01, and (b) I02, are the first frame of MPEG I-Visual test video sequences “Cars” [59] and “Matryoshka” [62], respectively; (c)-(u) are images from “FPI2k”, which are (c) I03, Box-1; (d) I04, Box 7; (e) I05, Box-28; (f) I06, Building_block_5; (g) I07, Building_block_86; (h) I08, Building_block_141; (i) I09, Calendar_9; (j) I10, Door_8; (k) I11, Indicator_6; (l) I12, Laboratory_65; (m) I13, Matryoshka_93; (n) I14, Matryoshka_169; (o) I15, Matryoshka_170; (p) I16, Plush toy_135; (q) I17, Toy car_1; (r) I18, Toy car_197; (s) I19, Toy car_502; (t) I20, Tree_29.

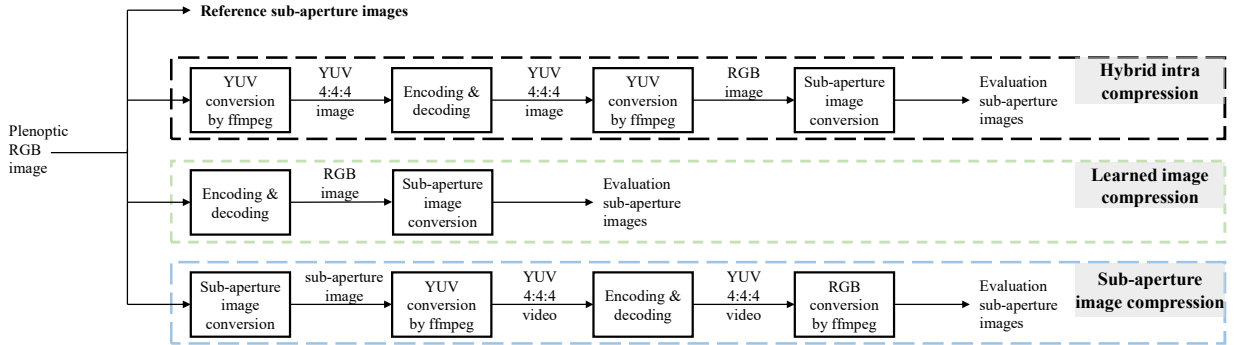


Fig. 10. Test flow chart for focused plenoptic image compression performance comparison following the common test conditions in MPEG lenslet video coding [5]. The sub-aperture images rendered from original plenoptic images are set as the reference to compute average distortion. The conversion and compression flow of hybrid intra codecs, learned plenoptic image compression and sub-aperture image compression methods are circled by black-dashed rectangle, green-dashed rectangle and blue-dashed rectangle, respectively.

$$PSNR = \frac{1}{5 \times 5} \sum_{k=1}^5 \sum_{j=1}^5 PSNR(i, j)$$

$$MS-SSIM = \frac{1}{5 \times 5} \sum_{k=1}^5 \sum_{j=1}^5 MS-SSIM(i, j)$$
(4)

where $PSNR(i, j)$ / $MS-SSIM(i, j)$ is the objective PSNR/MS-SSIM metric computed for the $(i, j)^{th}$ sub-aperture image. The RD performance is measured in terms of BD-rate [66]. The bitrate is defined by bit-per-pixel (bpp) which is calculated via dividing the number of bits by the total number of pixels of the original plenoptic image.

C. Experimental Results

1) *Rate-distortion Performance:* The compression efficiency of the proposed data preprocessing scheme and network are evaluated objectively in this subsection. First, the efficiency comparison of the original and preprocessed plenoptic images

TABLE II TESTING CASES AND CODING CONFIGURATION		
Input format	Testing cases	Configuration
Sub-aperture images	HEVC+SOP	“HEVC” + raster scan order proposed in [26] with Low Delay profile
	HEVC+SPR	“HEVC” + spiral scan order proposed in [27] with Low Delay profile
Original plenoptic images (OPI)	HEVC+OPI	“HEVC” RExt intra profile [63]
	CSP+OPI	method CSP proposed in [16]
	IIP	method IIP proposed in [18]
	ZIIP	method + SCC profile proposed in [17]
	SCC+OPI	“HEVC-SCC” intra profile [64]
	VVC+OPI	“VVC” intra profile [65]
Preprocessed plenoptic images (PPI)	HEVC+PPI	“HEVC” RExt intra profile [63]
	CSP+PPI	method proposed in [16]
	SCC+PPI	“HEVC-SCC” intra profile [64]
	VVC+PPI	“VVC” intra profile [65]
	Factor	method proposed in [34]
	Hyper	method proposed in [35]
	Joint	method proposed in [37]
	Attention	method proposed in [36]
Proposed	proposed network	

on different hybrid standards is listed in Table III. It can be found that the preprocessed images can improve compression efficiency significantly. As shown in the table, the data preprocessing scheme can achieve 40.24%, 34.58%, 43.96%, and 35.95% bitrate reduction on average for HEVC, CSP mode, SCC, and VVC intra coding, respectively, because preprocessed plenoptic images discard 48.98% sub-aperture image ineffective pixels from original plenoptic images. Besides, the HEVC intra coding on preprocessed images shows superior compression efficiency compared to VVC intra coding on original images with an average of 17.47% bitrate reduction.

Secondly, the compression efficiency of the proposed network combined with the data preprocessing scheme is evaluated in Table IV. As shown in the table, the proposed method can save 76.92% and 74.37% bitrate on average compared to SOTA focused plenoptic image compression methods *IIP* and *ZIIP*, respectively. And, the proposed method achieves an average bitrate reduction of 62.57%, 62.92%, 53.28%, and 51.67% bitrate saving compared to HEVC, CSP, SCC, and VVC intra coding on preprocessed plenoptic images, respectively. Furthermore, it outperforms Ballé *et al.* [34], Ballé *et al.* [35], Minnen *et al.* [37], and Cheng *et al.* [36] by 62.66%, 52.44%, 36.54%, and 18.73% bitrate reduction, respectively. The efficiency improvement between the proposed method and *Attention* reveals the proposed global attention module with large receptive field is more beneficial than the local attention mechanism to the plenoptic image compression. It can be found that the proposed method performs worse than *HEVC+SPR* on test image I01, I02, I10, and I20 in Table IV. The reason for the inferior performance lies in two aspects. One reason is that objects and the camera are far from each other resulting in a small disparity among the views and the scenes in I01, I02, I10, and I20 are captured with much less texture which is beneficial to the conventional inter-prediction architecture that exploits interview correlation among the reordered sub-aperture images.

TABLE III
BD-RATE COMPARISON AMONG THE ORIGINAL AND PREPROCESSED PLENOPTIC IMAGE COMPRESSION METHODS

Images	<i>HEVC+PPI</i>	<i>CSP+PPI</i>	<i>SCC+PPI</i>	<i>VVC+PPI</i>	<i>HEVC+PPI</i>
	vs. <i>HEVC+OPI</i>	vs. <i>CSP+OPI</i>	vs. <i>SCC+OPI</i>	vs. <i>VVC+OPI</i>	vs. <i>VVC+OPI</i>
I01	-40.3%	-34.0%	-42.6%	-37.6%	-22.0%
I02	-39.9%	-37.1%	-45.4%	-37.9%	-20.2%
I03	-43.0%	-37.3%	-45.7%	-38.3%	-20.3%
I04	-39.0%	-30.8%	-41.2%	-34.0%	-12.4%
I05	-43.8%	-31.8%	-46.9%	-39.3%	-20.4%
I06	-40.0%	-34.7%	-42.9%	-34.0%	-14.6%
I07	-45.3%	-38.7%	-46.9%	-40.6%	-23.1%
I08	-44.5%	-39.9%	-46.3%	-39.9%	-21.6%
I09	-38.3%	-31.7%	-42.7%	-33.8%	-14.6%
I10	-38.8%	-33.1%	-42.8%	-35.3%	-16.7%
I11	-35.8%	-29.9%	-42.0%	-31.7%	-16.7%
I12	-41.5%	-37.2%	-46.9%	-38.4%	-22.4%
I13	-41.4%	-35.7%	-44.9%	-35.9%	-16.2%
I14	-39.7%	-34.5%	-42.1%	-34.7%	-13.8%
I15	-42.9%	-37.6%	-45.7%	-38.4%	-18.3%
I16	-37.6%	-32.2%	-41.1%	-33.2%	-15.3%
I17	-36.0%	-30.4%	-42.6%	-31.9%	-10.6%
I18	-38.4%	-32.6%	-42.3%	-33.0%	-11.6%
I19	-42.3%	-36.9%	-44.2%	-37.2%	-18.1%
I20	-36.2%	-35.5%	-43.9%	-33.9%	-20.4%
Avg.	-40.24%	-34.58%	-43.96%	-35.95%	-17.47%

It can be proved that the proposed method can achieve 66.5% bitrate reduction compared to *HEVC+SPR* on I18 taken from a close shooting distance while our method achieves 56.0% bitrate increment compared to *HEVC+SPR* on I10 taken from outdoors. The other reason is that preprocessed plenoptic images contain more information ($d = 48 > d_{\min} = 40$) with a total 44% pixel increment than the internal regions of cropped microimages to render images.

TABLE IV
BD-RATE COMPARISON FOR PROPOSED METHOD

Images	<i>Proposed</i>											
	vs. <i>IIP</i>	vs. <i>ZIIP</i>	vs. <i>HEVC+PPI</i>	vs. <i>CSP+PPI</i>	vs. <i>SCC+PPI</i>	vs. <i>VVC+PPI</i>	vs. <i>Factor</i>	vs. <i>Hyper</i>	vs. <i>Joint</i>	vs. <i>Attention</i>	vs. <i>HEVC+SOP</i>	vs. <i>HEVC+SPR</i>
I01	-65.1%	-60.6%	-45.5%	-45.9%	-32.1%	-31.9%	-50.3%	-35.1%	-22.8%	-10.9%	20.2%	38.1%
I02	-65.1%	-63.8%	-44.3%	-44.4%	-35.9%	-29.4%	-72.3%	-54.6%	-28.9%	-11.8%	22.9%	36.8%
I03	-81.5%	-79.4%	-67.6%	-68.0%	-60.5%	-57.6%	-62.5%	-54.8%	-39.3%	-18.6%	-57.5%	-51.9%
I04	-78.1%	-74.7%	-66.1%	-66.5%	-55.3%	-55.3%	-64.2%	-53.9%	-36.1%	-20.0%	-27.7%	-16.7%
I05	-81.0%	-78.3%	-66.0%	-66.4%	-57.5%	-55.2%	-64.3%	-55.7%	-41.2%	-18.9%	-54.2%	-47.7%
I06	-81.1%	-78.0%	-68.2%	-68.6%	-59.1%	-58.3%	-65.9%	-57.1%	-42.0%	-21.2%	-51.1%	-43.8%
I07	-82.4%	-79.4%	-68.5%	-68.8%	-59.1%	-57.8%	-65.7%	-56.3%	-40.1%	-18.1%	-50.0%	-43.0%
I08	-80.1%	-78.2%	-64.3%	-64.7%	-57.8%	-53.5%	-63.1%	-53.6%	-38.0%	-14.5%	-68.9%	-64.9%
I09	-79.1%	-76.9%	-66.9%	-67.3%	-58.2%	-57.5%	-61.2%	-53.1%	-37.9%	-22.6%	-24.6%	-13.7%
I10	-67.9%	-66.6%	-54.8%	-55.3%	-43.6%	-41.2%	-56.9%	-46.4%	-32.3%	-20.6%	29.3%	56.0%
I11	-74.3%	-72.3%	-63.4%	-63.6%	-52.0%	-53.9%	-57.4%	-49.5%	-35.4%	-20.6%	-14.3%	-5.3%
I12	-75.0%	-72.4%	-55.4%	-55.8%	-46.2%	-43.8%	-56.7%	-45.3%	-27.5%	-13.5%	-40.0%	-29.7%
I13	-80.8%	-78.2%	-67.3%	-67.7%	-59.2%	-57.1%	-65.3%	-56.7%	-41.4%	-16.2%	-61.2%	-55.1%
I14	-87.1%	-85.5%	-78.3%	-78.6%	-73.2%	-71.5%	-62.8%	-55.0%	-38.7%	-18.2%	-42.1%	-34.2%
I15	-81.3%	-79.2%	-67.4%	-67.9%	-60.0%	-56.3%	-75.7%	-69.3%	-54.9%	-36.1%	-67.1%	-61.2%
I16	-77.1%	-75.0%	-63.6%	-63.9%	-55.7%	-54.0%	-60.1%	-51.2%	-35.1%	-17.2%	-36.5%	-27.6%
I17	-72.1%	-66.6%	-57.5%	-57.8%	-40.8%	-43.8%	-61.5%	-47.7%	-33.8%	-16.8%	-22.6%	-12.4%
I18	-78.3%	-76.4%	-65.7%	-66.2%	-57.9%	-55.0%	-67.7%	-56.0%	-38.9%	-17.7%	-70.9%	-66.5%
I19	-79.6%	-77.6%	-65.5%	-65.8%	-58.6%	-55.3%	-63.4%	-54.6%	-36.8%	-20.0%	-58.0%	-51.9%
I20	-71.3%	-68.3%	-55.0%	-55.2%	-42.9%	-45.0%	-56.1%	-42.9%	-29.7%	-21.1%	-5.6%	6.5%
Avg.	-76.92%	-74.37%	-62.57%	-62.92%	-53.28%	-51.67%	-62.66%	-52.44%	-36.54%	-18.73%	-34.00%	-24.41%

The RD curves of I01 “Cars” and I15 “Matryoshka_170” of 6 original plenoptic image compression testing cases including *HEVC+OPI*, *IIP*, *ZIPP*, *CSP+OPI*, *SCC+OPI*, and *VVC+OPI* are depicted in Fig. 11 accompanying with the proposed network. Although *VVC+OPI* achieves the best compression efficiency on 2 test images compared to the plenoptic image compression methods in terms of PSNR and MS-SSIM, the big performance gap between the proposed method and *VVC+OPI* demonstrates the superiority of the proposed method. To the best of our knowledge, our work is the first learned work to achieve better performance than the *VVC* intra compression on focused plenoptic image compression.

The compression efficiency among the 4 hybrid testing cases and 5 learned methods on preprocessed plenoptic images is shown in Fig. 12. The proposed method achieves the best performance compared to the hybrid codecs and learned image compression methods both on the metric of PSNR and MS-SSIM.

Two pseudo-video-based methods using zigzag and spiral scan order on HEVC are also compared, as shown in Fig. 13. The proposed method exhibits inferior compression performance at low bitrates (rate<0.2bpp) measured by PSNR and MS-SSIM, however, it manifests superior compression

performance at high bitrates (rate>0.2bpp) of PSNR on I01 “Cars”. Although the proposed method does not save bitrate when contrasted with reordering methods on I01 “Cars” in Table IV, it demonstrates promising compression performance at high test bitrates. On I15 “Matryoshka_170”, the proposed method surpasses HEVC reordering methods concerning PSNR and MS-SSIM at all test bitrates.

2) *Subjective Comparison Results*: To demonstrate our method can generate visually pleasant results, the central views of reconstructed I01 of 9 testing cases with approximately 0.06 bpp and a compression ratio of 400:1 are demonstrated in Fig. 14. Although the proposed network is optimized by MSE in Eq. (3) which prefers to produce smooth reconstructions, our method achieves comparable results with *HEVC+SOP*, and outperforms *HEVC+OPI*, *VVC+OPI*, *CSP+PPI*, *VVC+PPI*, *Factor*, and *Attention*. The stop sign marked in green rectangle generated by our method appears much more natural than the other codecs. Besides, more details are preserved by our method for the texture regions, as shown in the enlarged background regions in Fig. 14.

3) *Execution Time Comparison Results*: To evaluate the computational complexity of the proposed technique, a comparison with the traditional codecs *HEVC+PPI*, *VVC+PPI*,

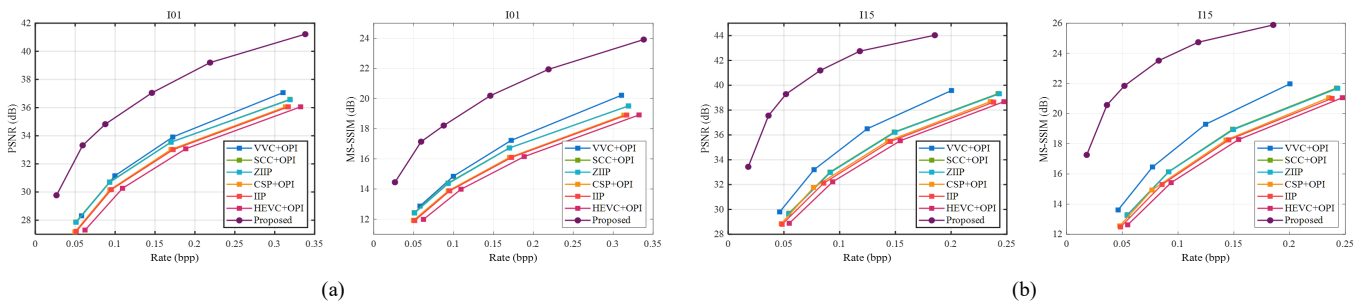


Fig. 11. RD performance evaluation of proposed network and original plenoptic image compression testing cases on (a) I01 “Cars” and (b) I15 “Matryoshka_170”.

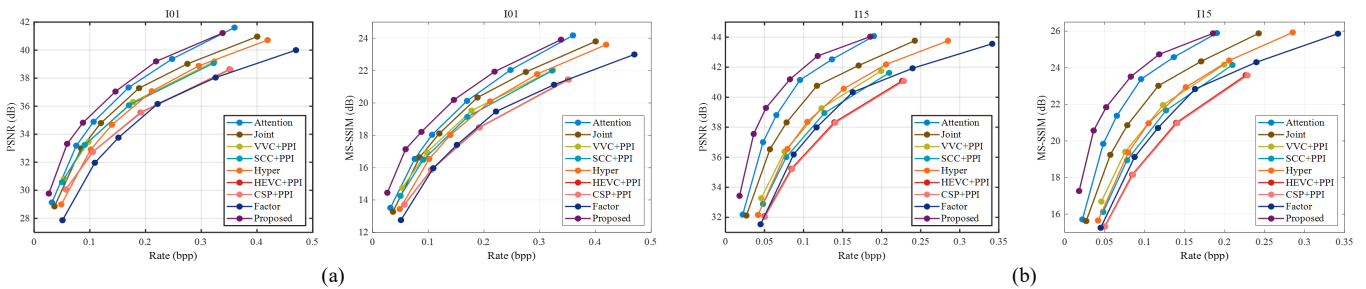


Fig. 12. RD performance evaluation of proposed network and preprocessed plenoptic image compression testing cases on (a) I01 “Cars” and (b) I15 “Matryoshka_170”.

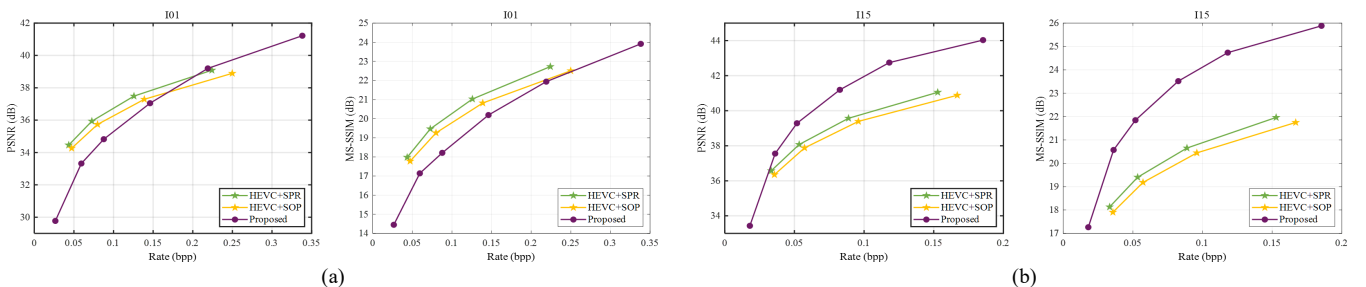


Fig. 13. RD performance evaluation of proposed network and sub-aperture-image-based compression testing cases on (a) I01 “Cars” and (b) I15 “Matryoshka_170”.



Fig. 14. Visualization of the central view of reconstructed plenoptic image I01 “Cars”. Three selected areas are marked by green, blue and red rectangles respectively. The metrics are [bpp ↓ /PSNR ↑ /MS-SSIM ↑].

TABLE V
EXECUTION TIME AND RELATIVE RATIOS OF DIFFERENT CODING METHODS AT FOUR RATES

Rate	Execution time				Execution time ratio			
	<i>HEVC+PPI</i>	<i>VVC+PPI</i>	<i>HEVC+SPR</i>	<i>Proposed</i>	<i>Proposed</i> vs. <i>HEVC+PPI</i>	<i>Proposed</i> vs. <i>VVC+PPI</i>	<i>Proposed</i> vs. <i>HEVC+SPR</i>	
Encoding Time	r_1	87.45s	306.09s	324.21s	273.33s	3.12	0.89	0.84
	r_2	92.42s	574.52s	368.82s	252.32s	2.72	0.44	0.68
	r_3	99.02s	950.51s	428.77s	253.00s	2.55	0.27	0.59
	r_4	107.89s	1315.05s	508.77s	260.34s	2.41	0.20	0.51
	Avg.	96.70s	786.54s	407.64s	259.75s	2.70	0.45	0.66
Decoding Time	r_1	0.33s	0.52s	0.80s	372.57s	1096.45	715.80	461.02
	r_2	0.38s	0.61s	0.89s	339.29s	884.73	552.28	378.09
	r_3	0.45s	0.80s	1.019s	338.97s	741.73	422.11	332.60
	r_4	0.49s	0.98s	1.15s	354.37s	713.30	361.48	305.89
	Avg.	0.41s	0.72s	0.97s	351.30s	859.05	512.92	369.40

and *HEVC+SPR* is conducted in terms of encoding and decoding time. All the testing cases are performed on the same machine equipped with Intel(R) Core(TM) i7-9700 CPU @ 3.00 GHz, 16GB RAM, and 64-bit Windows 10 operating system. The proposed method employs the same and isomorphic encoder and decoder which yields similar encoding and decoding time for different fixed-rate models. However, the encoding and decoding time differ when using different quantization parameters in traditional codecs. Four bitrates, labeled as r_1 , r_2 , r_3 , and r_4 from low to high bitrate, are used for execution time comparison. The quantization parameters used for *HEVC+PPI* and *VVC+PPI* are 42, 37, 32, and 27; for *HEVC+SPR*, they are 31, 28, 25, and 22 to match the target bitrates. The proposed method uses fixed-rate models with Lagrange multiplier values of 0.005, 0.025, 0.05, and 0.1. The average execution time of each testing case and relative ratios between the proposed method and other testing cases under four bitrates on 20 test images are summarized in Table V. As listed in the table, although the encoding complexity of the proposed method presents an average of 2.7 times higher than that of *HEVC+PPI*, more than 60% of bitrate reduction can be

achieved, as listed in Table IV. Its encoding complexity is 2.22 times and 1.51 times lower than that of *VVC+PPI* and *HEVC+SPR*, respectively, with much higher compression efficiency, which is very beneficial to applications. Currently, its decoding complexity is much higher than that of *HEVC+PPI*, *VVC+PPI*, and *HEVC+SPR*, which is mainly caused by the strict serial entropy coding modeling. This problem may be solved by applying advanced parallelization-friendly entropy coding methods [49, 67], which will be investigated further.

D. Ablation Study

To demonstrate the effectiveness of the proposed global attention module, we train and test the proposed network without global attention as baseline denoted as *Proposed w/o GA*. As shown in Fig. 15, the global attention module improves the compression efficiency by a large margin on the metrics of PSNR and MS-SSIM. Since the global attention module reduces bitrate consumption with similar distortion in the baseline, it proves that proposed module can capture the global information among feature maps to generate compact representation to improve compression efficiency. The superiority of global

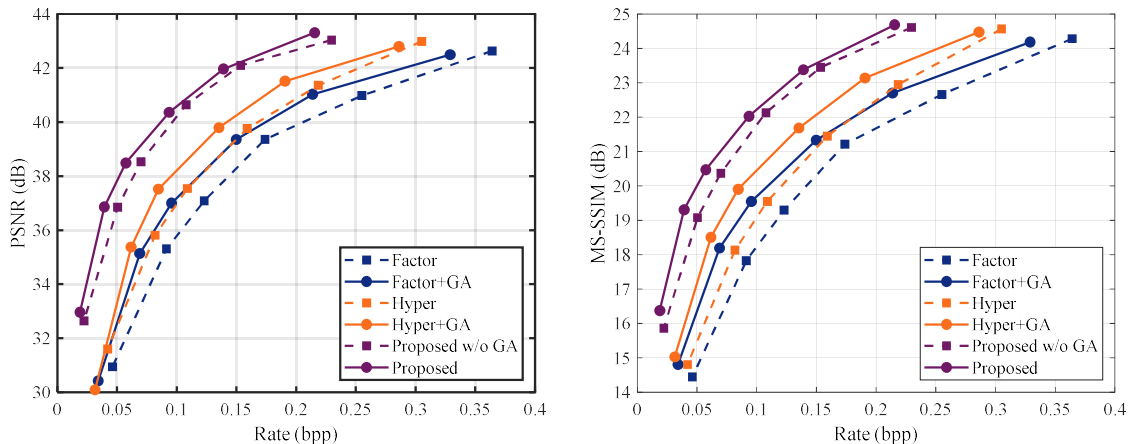


Fig. 15. Average RD performance evaluation of ablation study for global attention module on 20 test images.

attention module lies in two core aspects. One is that the global attention module has a particularly large receptive field to capture the dependencies of the microimages, and the other is that pixel-wise vector attention can compute the correlation of the distinctive pixel distribution of object response in unfocused depths.

To demonstrate the generality of the proposed module, we insert the global attention module in the third resampling structure of the main autoencoder and the first resampling operation of the hyper autoencoder in Ballé *et al.* [34] and Ballé *et al.* [35] similar to the proposed network. The modified networks are denoted as *Factor+GA* and *Hyper+GA* in Fig. 15. Compared to the baselines, the compression efficiency is also improved greatly for *Hyper+GA* and *Factor+GA* on test images in terms of PSNR and MS-SSIM, as shown in Fig. 15. And *Factor+GA* enhanced by the proposed global attention module achieves comparable results with *Hyper*. The performance improvement indicates that the global attention module can work as a plug-and-play component to enhance the existing models for plenoptic image compression.

VII. CONCLUSIONS

In this paper, a lossy end-to-end network with the global attention module is proposed for focused plenoptic image efficient compression. First, a sub-aperture image lossless preprocessing scheme is designed according to the imaging principle to reshape the sub-aperture image effective pixels in each microimage and align the cropped microimages to the rectangular grid. Then, the proposed global attention module with large receptive field draws the global dependencies from the input feature maps in the resampling process to improve compression efficiency. Also, an image dataset with 1910 focused plenoptic images captured in real circumstances is built for model robust training and testing.

The proposed network achieves superior coding performance in compressing preprocessed plenoptic images in terms of the metric of PSNR and MS-SSIM compared to the existing SOTA coding standards including HEVC, HEVC SCC, and VVC with an average of 62.57%, 53.28%, and 51.67% bitrate reduction, respectively. And, it is the first learned work that shows better results than VVC intra coding on the focused plenoptic image

compression. Our method outperforms the SOTA learned image compression model with 18.73% bitrate saving. Besides, the proposed method achieves comparable performance or even better with sub-aperture image compression on HEVC in terms of PSNR and MS-SSIM. The ablation study results reveal the effectiveness of the proposed global attention module which can work as a plug-and-play component to enhance the existing models for plenoptic image compression. For a different focused plenoptic camera, the values of its focal lengths of the main lens and microlens and the radius of each microlens are needed to change the EPA radius coefficient, cutting size in the proposed preprocessing, and the size of training patches containing the complete microimages for the network training and inference. Then, the network should be retrained to adapt network parameters to the variation in the intensity distribution. In the future, we will improve the size and diversity of the image dataset to promote the relative research fields. Also, we will explore other factors that utilize the distinctive distribution of focused plenoptic images to improve the compression efficiency, such as the local attention mechanism with a large receptive field with dilation convolution.

REFERENCES

- [1] T. G. Georgiev and A. Lumsdaine, "Focused plenoptic camera and rendering," *Journal of electronic imaging*, vol. 19, no. 2, pp. 1-11, 2010.
- [2] R. Ng, M. Levoy, M. Brédif, G. Duval, M. Horowitz, and P. Hanrahan, "Light field photography with a hand-held plenoptic camera," Stanford University, 2005.
- [3] X. Sun, X. Jin, T. Zhong, and P. Wang, "[MPEG-I Visual] A New Self-designed Focused Plenoptic Camera and the Captured Video Sequence "Boys",", ISO/IEC JTC1/SC29/WG11 MPEG2019 M46259, pp. 1-5, Marrakesh Morocco, Jan. 2019.
- [4] X. Jin, K. Tong, E. S. Jang, T. Fujii, G. Lafruit, and M. Teratani, "Draft Use Cases and Requirements of Lenslet Video Coding(LVC) for Dense Light Fields (DLF)," ISO/IEC JTC1/SC29/WG11 M58377, pp. 1-9, Online, Oct. 2021.
- [5] N0184, "Exploration Experiments and Common Test Conditions for Dense Light Fields," ISO/IEC JTC 1/SC 29/WG 04, pp. 1-7, Online, Jan. 2022.
- [6] M. Teratani and X. Jin, "AhG on Lenslet Video Coding (LVC)," ISO/IEC JTC 1/SC 29/WG 04 M58466, pp. 1-5, Online, Jan. 2022.
- [7] P. Schelkens et al., "JPEG Pleno light field coding technologies," in *Applications of Digital Image Processing XLII*, 2019, vol. 11137: SPIE, pp. 391-401.

- [8] L. F. Lucas et al., "Locally linear embedding-based prediction for 3D holoscopic image coding using HEVC," in 2014 22nd European Signal Processing Conference (EUSIPCO), 2014: IEEE, pp. 11-15.
- [9] C. Conti, P. Nunes, and L. D. Soares, "Light field image coding with jointly estimated self-similarity bi-prediction," *Signal Processing: Image Communication*, vol. 60, pp. 144-159, 2018.
- [10] C. Conti, P. Nunes, and L. D. Soares, "HEVC-based light field image coding with bi-predicted self-similarity compensation," in 2016 IEEE International Conference on Multimedia & Expo Workshops (ICMEW), 2016: IEEE, pp. 1-4.
- [11] R. J. Monteiro, P. J. Nunes, N. M. Rodrigues, and S. M. Faria, "Light field image coding using high-order intrablock prediction," *IEEE Journal of Selected Topics in Signal Processing*, vol. 11, no. 7, pp. 1120-1131, 2017.
- [12] D. Liu, P. An, R. Ma, W. Zhan, X. Huang, and A. A. Yahya, "Content-based light field image compression method with Gaussian process regression," *IEEE Transactions on Multimedia*, vol. 22, no. 4, pp. 846-859, 2019.
- [13] X. Zhang, H. Wang, and T. Tian, "Light field image coding with disparity correlation based prediction," in 2018 IEEE Fourth International Conference on Multimedia Big Data (BigMM), 2018: IEEE, pp. 1-6.
- [14] X. Jin, H. Han, and Q. Dai, "Plenoptic image coding using macropixel-based intra prediction," *IEEE Transactions on Image Processing*, vol. 27, no. 8, pp. 3954-3968, 2018.
- [15] H. Han, X. Jin, and Q. Dai, "Lenslet image compression based on image reshaping and macro-pixel Intra prediction," in 2017 IEEE International Conference on Multimedia and Expo (ICME), 2017: IEEE, pp. 1177-1182.
- [16] H. Han, X. Jin, and Q. Dai, "Lenslet image compression using adaptive macropixel prediction," in 2017 IEEE International Conference on Image Processing (ICIP), 2017: IEEE, pp. 4008-4012.
- [17] X. Jin, F. Jiang, L. Li, and T. Zhong, "Plenoptic 2.0 Intra Coding Using Imaging Principle," *IEEE Transactions on Broadcasting*, vol. 68, no. 1, pp. 110-122, 2021.
- [18] L. Li, X. Jin, and T. Zhong, "Imaging-Correlated Intra Prediction for Plenoptic 2.0 Video Coding," in 2020 IEEE International Conference on Multimedia and Expo (ICME), 2020: IEEE, pp. 1-6.
- [19] F. Jiang, X. Jin, and K. Tong, "Pixel Gradient Based Zooming Method for Plenoptic Intra Prediction," in 2021 International Conference on Visual Communications and Image Processing (VCIP), 2021: IEEE, pp. 1-5.
- [20] F. Jiang, X. Jin, and T. Zhong, "Zoomable Intra Prediction for Multi-Focus Plenoptic 2.0 Video Coding," in 2021 IEEE International Conference on Image Processing (ICIP), 2021: IEEE, pp. 2029-2033.
- [21] N. Bakir, W. Hamidouche, O. Déforges, K. Samrouth, and M. Khalil, "Light field image compression based on convolutional neural networks and linear approximation," in 2018 25th IEEE International Conference on Image Processing (ICIP), 2018: IEEE, pp. 1128-1132.
- [22] X. Huang, P. An, Y. Chen, D. Liu, and L. Shen, "Low Bitrate Light Field Compression with Geometry and Content Consistency," *IEEE Transactions on Multimedia*, vol. 24, pp. 152-165, 2022, doi: 10.1109/TMM.2020.3046860.
- [23] D. Liu, L. Wang, L. Li, Z. Xiong, F. Wu, and W. Zeng, "Pseudo-sequence-based light field image compression," in 2016 IEEE International Conference on Multimedia & Expo Workshops (ICMEW), 2016: IEEE, pp. 1-4.
- [24] W. Ahmad, S. Vagharshakyan, M. Sjöström, A. Gotchev, R. Bregovic, and R. Olsson, "Shearlet transform-based light field compression under low bitrates," *IEEE Transactions on Image Processing*, vol. 29, pp. 4269-4280, 2020.
- [25] P. Astola and I. Tabus, "Wasp: Hierarchical warping, merging, and sparse prediction for light field image compression," in 2018 7th European Workshop on Visual Information Processing (EUVIP), 2018: IEEE, pp. 1-6.
- [26] F. Dai, J. Zhang, Y. Ma, and Y. Zhang, "Lenselet image compression scheme based on subaperture images streaming," in 2015 IEEE International Conference on Image Processing (ICIP), 2015: IEEE, pp. 4733-4737.
- [27] A. Vieira, H. Duarte, C. Perra, L. Tavora, and P. Assuncao, "Data formats for high efficiency coding of lytro-illum light fields," in 2015 international conference on image processing theory, tools and applications (IPTA), 2015: IEEE, pp. 494-497.
- [28] C. Perra and P. Assuncao, "High efficiency coding of light field images based on tiling and pseudo-temporal data arrangement," in 2016 IEEE International Conference on Multimedia & Expo Workshops (ICMEW), 2016: IEEE, pp. 1-4.
- [29] M. U. Mukati and S. Forchhammer, "EPIC: Context adaptive lossless light field compression using epipolar plane images," in 2020 Data Compression Conference (DCC), 2020: IEEE, pp. 43-52.
- [30] X. Jiang, M. Le Pendu, R. A. Farrugia, S. S. Hemami, and C. Guillemot, "Homography-based low rank approximation of light fields for compression," in 2017 IEEE International Conference on Acoustics, Speech and Signal Processing (ICASSP), 2017: IEEE, pp. 1313-1317.
- [31] L. Li, Z. Li, B. Li, D. Liu, and H. Li, "Pseudo-sequence-based 2-D hierarchical coding structure for light-field image compression," *IEEE Journal of Selected Topics in Signal Processing*, vol. 11, no. 7, pp. 1107-1119, 2017.
- [32] D. Liu, X. Huang, W. Zhan, L. Ai, X. Zheng, and S. Cheng, "View synthesis-based light field image compression using a generative adversarial network," *Information Sciences*, vol. 545, pp. 118-131, 2021.
- [33] D. Liu, Y. Huang, Y. Fang, Y. Zuo, and P. An, "Multi-Stream Dense View Reconstruction Network for Light Field Image Compression," *IEEE Transactions on Multimedia*, pp. 1-16, 2022, doi: 10.1109/TMM.2022.3175023.
- [34] J. Ballé, V. Laparra, and E. P. Simoncelli, "End-to-end optimized image compression," arXiv preprint arXiv:1611.01704, 2016.
- [35] J. Ballé, D. Minnen, S. Singh, S. J. Hwang, and N. Johnston, "Variational image compression with a scale hyperprior," arXiv preprint arXiv:1802.01436, 2018.
- [36] Z. Cheng, H. Sun, M. Takeuchi, and J. Katto, "Learned image compression with discretized gaussian mixture likelihoods and attention modules," in Proceedings of the IEEE/CVF Conference on Computer Vision and Pattern Recognition, 2020, pp. 7939-7948.
- [37] D. Minnen, J. Ballé, and G. D. Toderici, "Joint autoregressive and hierarchical priors for learned image compression," *Advances in neural information processing systems*, vol. 31, 2018.
- [38] G. D. O. Alves et al., "The JPEG Pleno light field coding standard 4D-transform mode: How to design an efficient 4D-native codec," *IEEE Access*, vol. 8, pp. 170807-170829, 2020.
- [39] G. Jiang, X. Jin, K. Tong, X. Sun, T. Senoh, and M. Teratani, "[LVC][DLF] Method of Converting Tsinghua Plenoptic Image to Multiview Image," *ISO/IEC JTC1/SC29/WG04 M58758*, pp. 1-7, Online, Jan. 2022.
- [40] X. Sun, X. Jin, W. Ouyang, M. Teratani, and T. Fujii, "[MPEG-I Visual] Rendering algorithm for Tsinghua Single-focused Plenoptic Camera," *ISO/IEC JTC1/SC29/WG11 MPEG2019 M49008*, Gothenburg, Sweden, Jul. 2019.
- [41] G. Teniu and J. Ridge, "Market and practical considerations for Lenslet Video Coding – Preliminary report," *ISO/IEC JTC1/SC29/WG02 M59163*, Online, Jan. 2022.
- [42] T. Zhong, X. Jin, L. Li, and Q. Dai, "Light field image compression using depth-based CNN in intra prediction," in ICASSP 2019-2019 IEEE International Conference on Acoustics, Speech and Signal Processing (ICASSP), 2019: IEEE, pp. 8564-8567.
- [43] T. Zhong, X. Jin, and K. Tong, "3D-CNN autoencoder for plenoptic image compression," in 2020 IEEE International Conference on Visual Communications and Image Processing (VCIP), 2020: IEEE, pp. 209-212.
- [44] K. Tong, X. Jin, C. Wang, and F. Jiang, "SADN: Learned Light Field Image Compression with Spatial-Angular Decorrelation," in ICASSP 2022-2022 IEEE International Conference on Acoustics, Speech and Signal Processing (ICASSP), 2022: IEEE, pp. 1870-1874.
- [45] Y. Li, M. Sjöström, R. Olsson, and U. Jennehag, "Coding of focused plenoptic contents by displacement intra prediction," *IEEE Transactions on Circuits and Systems for Video Technology*, vol. 26, no. 7, pp. 1308-1319, 2015.
- [46] J. Xu, R. Joshi, and R. A. Cohen, "Overview of the emerging HEVC screen content coding extension," *IEEE Transactions on Circuits and Systems for Video Technology*, vol. 26, no. 1, pp. 50-62, 2015.
- [47] R. Zou, C. Song, and Z. Zhang, "The Devil Is in the Details: Window-based Attention for Image Compression," in Proceedings of the IEEE/CVF Conference on Computer Vision and Pattern Recognition, 2022, pp. 17492-17501.
- [48] Y. Qian et al., "Learning accurate entropy model with global reference for image compression," arXiv preprint arXiv:2010.08321, 2020.
- [49] D. Minnen and S. Singh, "Channel-wise autoregressive entropy models for learned image compression," in 2020 IEEE International Conference on Image Processing (ICIP), 2020: IEEE, pp. 3339-3343.
- [50] G. K. Wallace, "The JPEG still picture compression standard," *IEEE transactions on consumer electronics*, vol. 38, no. 1, pp. 18-34, 1992.

- [51] D. Taubman and M. Marcellin, JPEG2000 image compression fundamentals, standards and practice: image compression fundamentals, standards and practice. Springer Science & Business Media, 2012.
- [52] G. J. Sullivan, J.-R. Ohm, W.-J. Han, and T. Wiegand, "Overview of the high efficiency video coding (HEVC) standard," IEEE Transactions on circuits and systems for video technology, vol. 22, no. 12, pp. 1649-1668, 2012.
- [53] B. Bross et al., "Overview of the versatile video coding (VVC) standard and its applications," IEEE Transactions on Circuits and Systems for Video Technology, vol. 31, no. 10, pp. 3736-3764, 2021.
- [54] X. Zhu, J. Song, L. Gao, F. Zheng, and H. T. Shen, "Unified Multivariate Gaussian Mixture for Efficient Neural Image Compression," in Proceedings of the IEEE/CVF Conference on Computer Vision and Pattern Recognition, 2022, pp. 17612-17621.
- [55] X. Sun, T. Zhong, X. Jin, and P. Wang, "[MPEG-I Visual] A new test sequence "Experimenting" captured by Tsinghua single-focused plenoptic camera," ISO/IEC JTC1/SC29/WG11 MPEG2019 M47620, pp. 1-3, Geneva, Switzerland, Mar. 2019.
- [56] D. G. Dansereau, O. Pizarro, and S. B. Williams, "Decoding, calibration and rectification for lenselet-based plenoptic cameras," in Proceedings of the IEEE conference on computer vision and pattern recognition, 2013, pp. 1027-1034.
- [57] A. Lumsdaine and T. Georgiev, "The focused plenoptic camera," in 2009 IEEE International Conference on Computational Photography (ICCP), 2009: IEEE, pp. 1-8.
- [58] G. Wu et al., "Light field image processing: An overview," IEEE Journal of Selected Topics in Signal Processing, vol. 11, no. 7, pp. 926-954, 2017.
- [59] X. Sun, T. Zhong, X. Jin, and P. Wang, "[MPEG-I Visual] A new test sequence "Cars" captured by Tsinghua single-focused plenoptic camera," ISO/IEC JTC1/SC29/WG11 MPEG2019 M49007, Gothenburg, Sweden, Jul. 2019
- [60] T. Senoh et al., "[LVC][DLF] Conversion of Multi-Focused Plenoptic 2.0 Lenslet Image to Multiview Image," ISO/IEC JTC 1/SC 29/WG 04 M57813, pp. 1-14, Online, Oct. 2021.
- [61] A. Vaswani et al., "Attention is all you need," Advances in neural information processing systems, vol. 30, 2017.
- [62] X. Sun, T. Zhong, K. Tong, and X. Jin, "[MPEG-I Visual] A new test sequence "Matryoshka" captured by Tsinghua plenoptic video camera," ISO/IEC JTC1/SC29/WG11 MPEG2020 M52250, pp. 1-3, Brussels, Belgium, Jan. 2020.
- [63] "HEVC Official Test Model." <https://vcgit.hhi.fraunhofer.de/jvct/HM/-/tags/HM-16.22> (accessed).
- [64] "HEVC SCC Official Test Model HM+SCM." <https://vcgit.hhi.fraunhofer.de/jvct/HM/-/tags/HM-16.9+SCM-8.0> (accessed).
- [65] "VVC Official Test Model." https://vcgit.hhi.fraunhofer.de/jvct/VVCSoftware_VTM/-/tree/VTM-10.0 (accessed).
- [66] G. Bjontegaard, "Calculation of average PSNR differences between RD-curves," VCEG-M33, 2001.
- [67] D. He, Y. Zheng, B. Sun, Y. Wang, and H. Qin, "Checkerboard context model for efficient learned image compression," in Proceedings of the IEEE/CVF Conference on Computer Vision and Pattern Recognition, 2021, pp. 14771-14780.



Kedeng Tong is currently pursuing the M.E. degree with Shenzhen International Graduate School, Tsinghua University. He has published several papers, e.g. ICASSP. His research interest is light-field compression, image compression.



Xin Jin (S'03–M'09–SM'11) received the M.S. degree in communication and information system and the Ph.D. degree in information and communication engineering, both from Huazhong University of Science and Technology, Wuhan, China, in 2002 and 2005, respectively.

From 2006 to 2008, she was a Postdoctoral Fellow with The Chinese University of Hong Kong. From 2008 to 2012, she was a Visiting

Lecturer with Waseda University, Fukuoka, Japan. Since Mar. 2012, she has been with Shenzhen International Graduate School, Tsinghua University, China, where she is currently a professor. Her current research interests include computational imaging and power-constrained video processing and compression. She has published over 170 conference and journal papers.

Dr. Jin is an IEEE Senior Member, and a member of SPIE and ACM. She is the Distinguished Professor of Pengcheng Scholar. She received Gold Medal of International Exhibition of Inventions of Geneva in 2022, the second prize of National Science and Technology Progress Award in 2016, the first prize of Guangdong science and technology award in 2015 and ISOC Best Paper Award in 2010.



Yuqing Yang is currently pursuing the M.E. degree with Shenzhen International Graduate School, Tsinghua University. His research interest is video compression.



Chen Wang is currently pursuing the M.E. degree with Shenzhen International Graduate School, Tsinghua University. His research interest is video compression.



Jinshi Kang is currently pursuing the M.E. degree with Shenzhen International Graduate School, Tsinghua University. His research interest is light field defect inspection.



Fan Jiang received the M.E. degree with Shenzhen International Graduate School, Tsinghua University. He has published several papers, e.g. ICIP, VCIP, and T.BC. His research interest is light-field compression.